Towards Mobile Mapping of Underground Mines

Andreas Nüchter, Jan Elseberg, Peter Janotta

Informatics VII – Robotics and Telematics
Julius-Maximilian University of Würzburg
Am Hubland, D-97074 Würzburg, Germany
andreas@nuechti.de

ABSTRACT:

Mobile laser scanning systems automate the acquisition of 3D point clouds of environments. The mapping systems are commonly mounted on cars or ships. This paper presents a flexible mapping solution mounted on an underground vehicle that is able to map underground mines in 3D in walking speeds. A clever choice of hard- and software enables the system to generate 3D maps without using GPS (global positioning system) information and without relying on highly expensive IMU (inertial measurement unit) systems.

Key words: Mobile laser scanning, underground mapping, SLAM.

1 Introduction

The increasing need for rapid characterization and quantification of complex environments has created challenges for data analysis. This critical need comes from many important areas, including the maintenance of underground tunnels and mines. 3D laser scanning is is able to acquire millions of 3D metric measurement points quickly. To this end, the scanner sends out a focused laser light and measures the time until a reflection reaches the sensor. The actual time-of-flight measurement is done either by pulsed laser light or modulated light. Actuating the sensor, or using rotating mirrors enable measurements in all directions.

Terrestrial laser scanner use sensor measurements at different poses, i.e., position and orientations, to reconstruct environments. Mobile laser scanner uses a scanner in profiler mode, i.e., only a single axis is actuated and a slice of the environment is measured. By moving the mapping system around, 3D environments can be digitized. Mobile mapping is the state of the art for the acquisition of 3D data using vehicles (kinematic laser scanning) or aircraft (airborne laser scanning). While terrestrial laser scanning produces 3D point clouds in a consistent manner, mobile mapping usually needs external position systems such as the global positioning system (GPS) for estimating the vehicle's trajectory. For terrestrial scans we have developed registration methods that register acquired 3D point clouds in a common coordinate systems, in an incremental fashion (Nüchter, A., Surmann, H., Lingemann, K., Hertzberg, J., and Thrun S., 2004) or in global consistent fashion (Borrmann, D., Elseberg, J., Lingemann, K., Nüchter, A., and Hertzberg, J., 2008), (Nüchter, A., Elseberg, J., Schneider, P., Paulus, D. 2010), that is using bundle adjustment for 3D point clouds. Progress in mobile mapping is obtained by using ideas from 3D scan matching in the area of kinematic laser scanning (Elseberg, J., Borrmann, D., and Nüchter, A., 2013), where the influence of inertial measurement units (IMUs) and GPS or Global Navigation Satellite System (GNSS) is reduced.

This paper presents results of the Measurement in Motion system, a laser scanning system, designed for GNSS-denied environments. A clever choice of hard- and software enables the system to generate 3D maps without using GPS (global positioning system) information and

2 The Measurement in Motion mapping system

The setup of the mapping system is strongly influenced by the robot Irma3D (Nüchter, A., Elseberg, J., Borrmann, D., 2013). The basis is a chassis where aluminum components and system solutions for building fixtures, so-called item24-profiles (item24 Industrietechnik, 2017) similar to the Volksbot RT 3 chassis have been attached Energy is currently provided by two 12 V lead-acid batteries, but to save weight, these will be replaced by lithium polymer batteries. Similarly to Irma3D (Nüchter, A., Elseberg, J., Borrmann, D., 2013), the system features a horizontally scanning SICK LMS 100, which is used to observe the motion of the carrier using a grid mapping variant. To fully exploit the 270â—¦ field of view of the SICK LMS 100, the sensor head is positioned slightly above the load carrier. Furthermore, the system features two vertically mounted SICK LMS100 sensors, however, which are not used in the presented study. The central sensor of the system is the 3D laser scanner RIEGL VZ-400. The VZ-400 is able to freely rotate around its vertical axis to acquire 3D scans. The system is also equipped with a network switch to receive the data from the two scanners and to connect the embedded PC with an Intel Celeron processor.

The Measurement in Motion mapping system was mounted on a car, cf. Figure 1, which was driven at walking speed. To ensure walking speed, the first and third author were walking in beside the car.

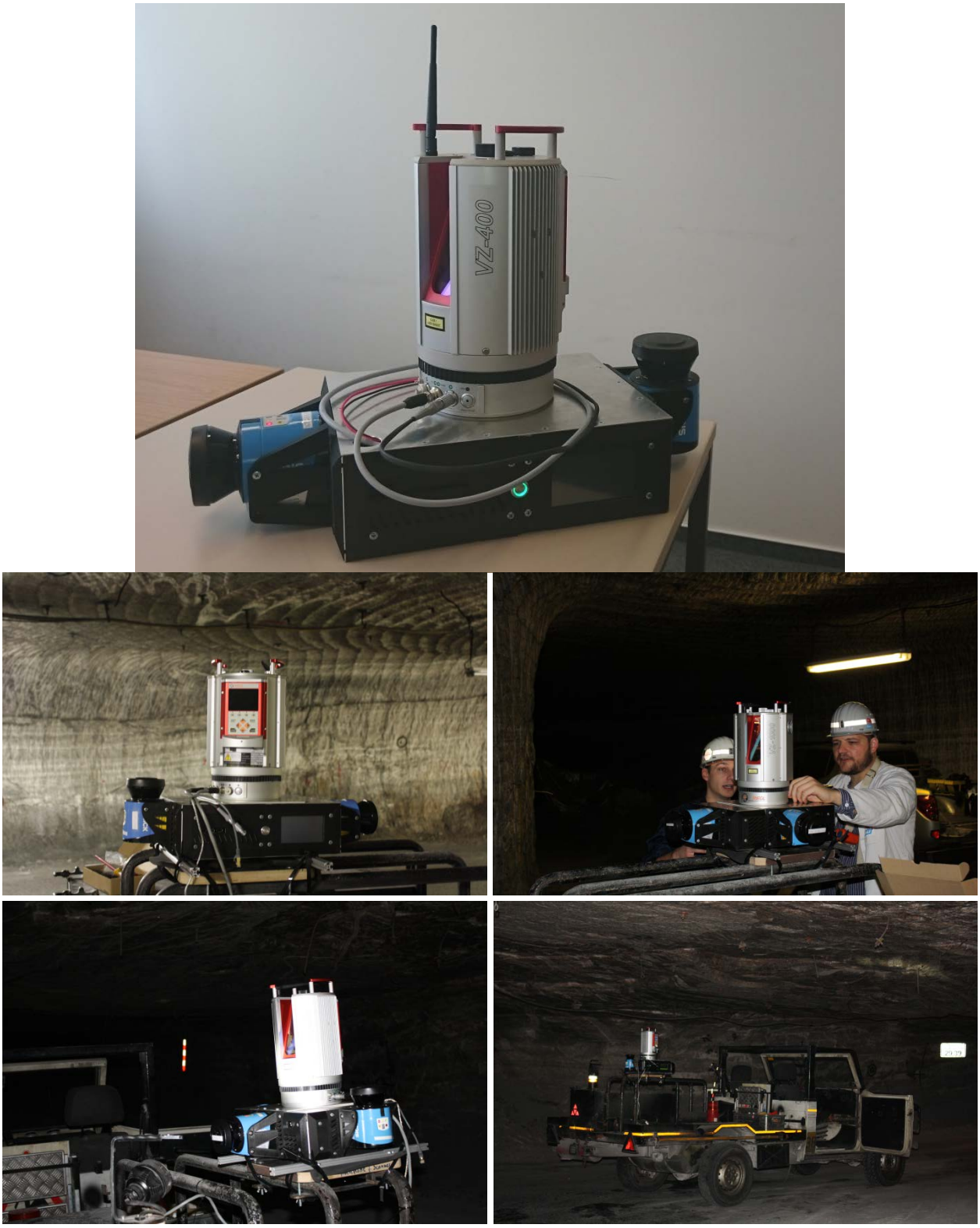

Fig. 1: Measurement in Motion Mapping System.

3 2D Mapping with the Horizontally-Mounted Laser Profiler and Initial Trajectory

HectorSLAM is a state of the art 2D SLAM solution (Kohlbrecher, S., Meyer, J., von Stryk, J., and Klingauf, U., 2011). It represents the environment in a 2D occupancy grid, which is a very well-known representation in Robotics. Compared to other state of the art grid mapping approaches, it neither uses feature extraction as in (Durrant-Whyte, H. and Bailey, T., 2006) nor a particle filter for mapping as in FastSLAM (Montemerlo, M., Thrun, S., Koller, D., and Wegbreit B., 2002), (Hähnel, D., Burgard, W., Fox, D., and Thrun S., 2003), which commonly enable reliable robot localization and mapping.

The 2D LiDAR performs 6 DoF motion while the system is driven. Usually, each scan has to be transformed into a local stabilized coordinate frame using an IMU-estimated attitude of the LiDAR system. As the system does not feature an IMU, this step is discarded in this scenario. In a scan matching process, the acquired scan is matched with the existing map. The optimization of the alignment is done using a Gauss-Newton approach, similar to the work in (Lucas, B. D. and Kanade T., 1981), and therefore neither data association, i.e., point matching, nor an exhaustive search for the optimal pose transformation is needed. As any hill climbing/gradient based approach has the inherent risk of getting stuck in local minima (Kohlbrecher, S., Meyer, J., von Stryk, J., and Klingauf, U., 2011) the developers of HectorSLAM mitigate it by employing a multi-resolution map representation similar to image pyramid approaches used in computer vision. Different maps are kept in memory and simultaneously updated using the pose estimates generated by the alignment process, which ensures consistency across scales. The scan alignment process is started at the coarsest map level and the resulting estimated pose is used as the start estimate for the next level. Overall, HectorSLAM has proven to produce a 2D map reliably.

Next, we shift our focus to processing the 3D data obtained by the Riegl scanner. We “unwind” the data using the HectorSLAM trajectory, split the 3D data into segments, match these segments and distribute the alignment in a semi-rigid fashion. In addition, we present our calibration method.

4 Mobile Mapping with Constantly Spinning Scanners

In the following subsections we summarize our work from (Borrmann, D., Elseberg, J., Lingemann, K., Nüchter, A., and Hertzberg, J., 2008) and (Elseberg, J., Borrmann, D., and Nüchter, A., 2013). These algorithms are suited to turn laser range data acquired with a rotating scanner while the acquisition system is in motion into precise, globally consistent 3D point clouds.

4.1 Automatic Calibration for Mobile Mapping

Calibration is the process of estimating the parameters of a system. In (Elseberg, J., Borrmann, D., and Nüchter, A., 2013) we presented a general method for this estimation problem, where the 3D point cloud represents samples from a probability density function $d(l)$ which represents the probability that a specific location l has been measured.

$$d(l) = \frac{1}{n}\sum_{j}^{n} G(l - p_j, \sigma^2 I) \quad (1)$$

where $G(\mu, \sigma^2 I)$ is a Gaussian distribution with mean μ and covariance $\sigma^2 I$. This is more than sufficient to capture consistency of a point cloud. As calibration errors lead to the same surfaces appearing at multiple positions in the point cloud, the entropy can be used to measure the compactness of the point cloud. (Sheehan, M., Harrison, A., Newman, P., 2011) derive the following simplified entropy measure, which depends on only the pairwise distance of every possible pair of sample points:

$$E'(P) \& = -\sum_{i}^{n}\sum_{j}^{n} G\left(p_i - p_j, 2\sigma^2 I\right)(l) \quad (2)$$

Considering the enormous amount of data, calculating a measure that uses all possible pairs of sample points seams infeasible. We use an octree-based reduction (Elseberg, J., Borrmann, D., and Nüchter, A., 2013) and use only closest point pairs to overcome the computational issues.

Our automatic method treats the "unwinding"-method as a function where the calibration parameters are the unknown variables. The function expresses how the trajectory, the laser measurements and the calibration parameters are combined to create the 3D point cloud. Finally, we employ Powell's method for optimizing the calibration parameters.

4.2 6D SLAM

For our system, we need a continuous-time SLAM solution, which is explained in the next section. To understand the basic idea, we summarize its basis, 6D SLAM. 6D SLAM works similarly to the well-known iterative closest points (ICP) algorithm, which minimizes the following error function

$$E(R, t) = \frac{1}{N}\sum_{i=1}^{N} \|m_i - (Rd_i + t)\| \quad (3)$$

to solve iteratively for an optimal rotation $\boldsymbol{T} = (\boldsymbol{R}, \mathbf{t})$, where the tuples $(\boldsymbol{m}_i, \boldsymbol{d}_i)$ of corresponding model M and data points D are given by minimal distance, i.e., mi is the closest point to $\boldsymbol{d}_i$ within a close limit (Besl, P. and McKay, D., 1992). Instead of the two-scan-Eq. (3), we look at the n-scan case:

$$E = \frac{1}{N}\sum_{j\to k}\sum_{i} \|(R_j m_i + t_j) - (R_k d_i + t_k)\| \quad (4)$$

where *j* and *k* refer to scans of the SLAM graph, i.e., to the graph modelling the pose constraints in SLAM or bundle adjustment. If they overlap, i.e., closest points are available, then the point pairs for the link are included in the minimization. We solve for all poses at the same time and iterate like

in the original ICP. For some applications it is necessary to have a notion of the uncertainty of the poses calculated by the registration algorithm. The following is the extension of the probabilistic approach first proposed by (Lu and Milios, 1997) to 6 DoF. This extension is not straightforward, since the matrix decomposition, i.e., Eq. (22) cannot be derived from first principles. For a more detailed description of these extensions refer to (Borrmann et al., 2008). In addition to the poses $\boldsymbol{X}_j$, the pose estimates $\bar{\boldsymbol{X}}_j$ and the pose errors $\Delta\boldsymbol{X}_j$ are required.

The positional error of two poses $\boldsymbol{X}_j$ and $\boldsymbol{X}_k$ is described by:

$$E_{k,j} = \sum_{i=1}^{m} \left\| \boldsymbol{X}_j \oplus \boldsymbol{d}_i - \boldsymbol{X}_k \oplus \boldsymbol{m}_i \right\| = \sum_{i=1}^{\mathrm{m}} \left\| \boldsymbol{Z}_i(\boldsymbol{X}_j, \boldsymbol{X}_k) \right\|^2 \qquad (5)$$

Here, $\oplus$ is the compounding operation that transforms a point into the global coordinate system. For small pose differences, $E_{k,j}$ can be linearized by use of a Taylor expansion:

$$\begin{aligned} \boldsymbol{Z}_i(\boldsymbol{X}_j, \boldsymbol{X}_k) \approx\ & \bar{\boldsymbol{X}}_j \oplus \boldsymbol{d}_i - \bar{\boldsymbol{X}}_k \oplus \boldsymbol{m}_i - (\nabla_j \boldsymbol{Z}_i(\bar{\boldsymbol{X}}_j, \bar{\boldsymbol{X}}_k)\Delta\boldsymbol{X}_j \\ & - \nabla_k \boldsymbol{Z}_i\,(\boldsymbol{X}_j, \bar{\boldsymbol{X}}_k)\Delta\boldsymbol{X}_k) \end{aligned} \qquad (6)$$

where ∇k denotes the derivative with respect to $\boldsymbol{X}_j$ and $\boldsymbol{X}_k$ respectively. Utilizing the matrix decompositions

$\boldsymbol{M}_i\boldsymbol{H}_j$ and $\boldsymbol{D}_j\boldsymbol{H}_k$ of the respective derivatives that separates the poses from the associated points gives:

$$\begin{aligned} \boldsymbol{Z}_i\,(\boldsymbol{X}_j, \boldsymbol{X}_k) &= \boldsymbol{Z}_i(\,\bar{\boldsymbol{X}}, \bar{\boldsymbol{X}}_k) - \left(\boldsymbol{M}_i\,\boldsymbol{H}_j\,\Delta\boldsymbol{X}_j - \boldsymbol{D}_i\,\boldsymbol{H}_k\,\Delta\,\boldsymbol{X}_k\,\right) \\ &= \boldsymbol{Z}_i(\bar{\boldsymbol{X}}, \boldsymbol{X}_k) - (\boldsymbol{M}_i\,\boldsymbol{X}'_j - \boldsymbol{D}_i\,\boldsymbol{X}'_k\,) \end{aligned} \qquad (7)$$

Appropriate decompositions are given for both the Euler angles and quaternion representation in the following paragraphs. Because $\boldsymbol{M}_i$ as well as $\boldsymbol{D}_i$ are independent of the pose, the positional error $\boldsymbol{E}_{j,k}$ is minimized with respect to the new pose difference $\boldsymbol{E}'$, i.e.,

$$\begin{aligned} \boldsymbol{E}_{j,k} &= (\boldsymbol{H}_j\,\Delta\,\boldsymbol{X}_j - \boldsymbol{H}_k\,\Delta\,\boldsymbol{X}_k \\ &= (\boldsymbol{X}'_j - \boldsymbol{X}'_k) \end{aligned} \qquad (8)$$

is linear in the quantities $\boldsymbol{X}_j$ that will be estimated so that the minimum of $\boldsymbol{E}_{j.k}$ and the correspoding covariance are given by

$$\bar{\boldsymbol{E}}_{j,k} = (\boldsymbol{M}^T\boldsymbol{M}^{-1})\boldsymbol{M}^T\boldsymbol{Z} \qquad (9)$$

$$\boldsymbol{C}_{j,k} = s\text{^}2\,(\boldsymbol{M}^T\boldsymbol{M}) \qquad (10)$$

where s^2 is the unbiased estimate of the covariance of the identically, independently distributed errors of $\boldsymbol{Z}$:

$$s^2 = \frac{(\boldsymbol{Z} - \boldsymbol{M}\bar{\boldsymbol{E}})^T(\boldsymbol{Z} - \boldsymbol{M}\bar{\boldsymbol{E}})}{(2m-3)}. \qquad (11)$$

Here $\boldsymbol{Z}$ is the concatenated vector consisting of all $\boldsymbol{Z}_i(\bar{\boldsymbol{X}}_j, \bar{\boldsymbol{X}}_k)$ and $\boldsymbol{M}$ the concatenation of all $\boldsymbol{M}_i$'s.

Up to now all considerations have been on a local scale. With the linearized error metric $\boldsymbol{E}'_{j,k}$ and the Gaussian distribution $\overline{\boldsymbol{E}}_{j,k}$, $\boldsymbol{C}_{j,k}$ a Mahalanobis distance that describes the global error of all the poses is constructed:

$$\begin{aligned}\boldsymbol{W} &= \sum_{j\to k}(\overline{\boldsymbol{E}}_{j,k}-\boldsymbol{E}'_{j,k})^{-1}\ \boldsymbol{C}_{j,k}^{-1}(\overline{\boldsymbol{E}}_{j,k}-\boldsymbol{E}'_{j,k}) \\ &= \sum_{j\to k}(\overline{\boldsymbol{E}}_{j,k}-(\boldsymbol{X}'_j-\boldsymbol{X}'_k))^{-1}\ \boldsymbol{C}_{j,k}^{-1}(\overline{\boldsymbol{E}}_{j,k}-(\boldsymbol{X}'_j-\boldsymbol{X}'_k))\end{aligned} \tag{12}$$

In matrix notation, $\boldsymbol{W}$ becomes:

$$\boldsymbol{W} = (\overline{\boldsymbol{E}}-\boldsymbol{H}\boldsymbol{X})^T\boldsymbol{C}^{-1}(\boldsymbol{E}^{-}-\boldsymbol{H}\boldsymbol{X}). \tag{13}$$

Here $\boldsymbol{H}$ is the signed incidence matrix of the pose graph, $\overline{\boldsymbol{E}}$ is the concatenated vector consisting of all $\overline{\boldsymbol{E}}'_{j,k}$ and $\boldsymbol{C}$ is a block-diagonal matrix comprised of $\boldsymbol{C}_{j,k}^{-1}$ as submatrices. Minimizing this function yields new optimal pose estimates. The minimization of $\boldsymbol{W}$ is accomplished via the following linear equation system:

$$(\boldsymbol{H}^T\boldsymbol{C}^{-1}\boldsymbol{H})\boldsymbol{X} = \boldsymbol{H}^T\boldsymbol{C}^{-1}\overline{\boldsymbol{E}} \tag{14}$$

$$\boldsymbol{B}\boldsymbol{X} = \boldsymbol{A}. \tag{15}$$

The matrix $\boldsymbol{B}$ consists of the submatrices

$$\boldsymbol{B}_{j,k} = \begin{cases}\sum_{k=0}^{n}\boldsymbol{C}_{j,k}^{-1} & (j=k)\\ \boldsymbol{C}_{j,k}^{-1} & (j=k)\end{cases} \tag{14}$$

The entries of $\boldsymbol{A}$ are given by:

$$\boldsymbol{A}_j = \sum_{\substack{k=0\\k\neq j}}^{n}\boldsymbol{C}_{j,k}^{-1}\ \overline{\boldsymbol{E}}_{j,k}. \tag{17}$$

In addition to $\boldsymbol{X}$, the associated covariance of $\boldsymbol{C}_X$ is computed as follows:

$$\boldsymbol{C}_X = \boldsymbol{B}^{-1} \tag{16}$$

Note that the results have to be transformed in order to obtain the optimal pose estimates.

$$\boldsymbol{X}_j = \overline{\boldsymbol{X}}_j - \boldsymbol{H}_j^{-1}\boldsymbol{X}'_j \tag{19}$$

$$\boldsymbol{C}_j = (\boldsymbol{H}_j^{-1}\boldsymbol{C}_j^X\left(\boldsymbol{H}_j^{-1}\right)^T. \tag{20}$$

The representation of pose $\boldsymbol{X}$ in Euler angles, as well as its estimate and error is as follows:

$$\boldsymbol{X} = \begin{pmatrix}t_x\\t_y\\t_z\\\theta_x\\\theta_x\\\theta_z\end{pmatrix}, \overline{\boldsymbol{X}} = \begin{pmatrix}\bar{t}_x\\\bar{t}_y\\\bar{t}_z\\\bar{\theta}_x\\\bar{\theta}_x\\\bar{\theta}_z\end{pmatrix}, \Delta\boldsymbol{X} = \begin{pmatrix}\Delta t_x\\\Delta t_y\\\Delta t_z\\\Delta\theta_x\\\Delta\theta_x\\\Delta\theta_z\end{pmatrix} \tag{21}$$

The matrix decomposition $\boldsymbol{M}_i\boldsymbol{H} = \nabla\boldsymbol{Z}_i\overline{\boldsymbol{X}}$ is given by

$$\boldsymbol{H} = \begin{pmatrix} 1 & 0 & 0 & 0 & \bar{t}_z\cos(\bar{\theta}_x) + \bar{t}_y\sin(\bar{\theta}_x) & \bar{t}_y\cos(\bar{\theta}_y)\cos(\bar{\theta}_x) - \bar{t}_z\cos(\bar{\theta}_x)\sin(\bar{\theta}_x) \\ 0 & 1 & 0 & -\bar{t}_z & -\bar{t}_x\sin(\bar{\theta}_x) & \bar{t}_x\cos(\bar{\theta}_x)\cos(\bar{\theta}_x) - \bar{t}_z\sin(\bar{\theta}_x) \\ 0 & 0 & 1 & \bar{t}_y & -\bar{t}_x\cos(\bar{\theta}_x) & \bar{t}_x\cos(\bar{\theta}_y)\sin(\bar{\theta}_x) + \bar{t}_y\sin(\bar{\theta}_y) \\ 0 & 0 & 0 & 1 & 0 & \sin(\bar{\theta}_y) \\ 0 & 0 & 0 & 0 & \sin(\bar{\theta}_x) & \cos(\bar{\theta}_x)\cos(\bar{\theta}_y) \\ 0 & 0 & 0 & 0 & \cos(\bar{\theta}_y) & -\cos(\bar{\theta}_y)\sin(\bar{\theta}_x) \end{pmatrix} \quad \textbf{(22)}$$

$$\boldsymbol{M}_i = \begin{pmatrix} 1 & 0 & 0 & 0 & -d_{y,i} & -d_{z,i} \\ 0 & 1 & 0 & d_{z,i} & d_{x,i} & 0 \\ 0 & 0 & 1 & -d_{y,i} & 0 & d_{x,i} \end{pmatrix} \quad \textbf{(23)}$$

As required, $\boldsymbol{M}_i$ contains all point information while $\boldsymbol{H}$ expresses the pose information. Thus, this matrix decomposition constitutes a pose linearization similar to those proposed in the preceding sections. Note that, while the matrix decomposition is arbitrary with respect to the column and row ordering of $\boldsymbol{H}$, this particular description was chosen due to its similarity to the 3D pose solution given in (Lu and Milios, 1997).

4.3 Continous-time SLAM for Trajectory Optimization

Unlike other state of the art algorithms, like (Stoyanov and Lilienthal, 2009) and (Bosse et al., 2012), our continuous-time SLAM algorithm is not restricted to purely local improvements. Our method makes no rigidity assumptions, except for the computation of the point correspondences. The method requires no explicit motion model of a vehicle for instance, thus it works well on back-pack systems. The continuous-time SLAM for trajectory optimization works in full 6 DoF. The algorithm requires no high-level feature computation, i.e., it requires only the points themselves.

In case of mobile mapping, one does not have separate terrestrial 3D scans. In the current state of the art in the robotics community developed by (Bosse et al., 2012) for improving overall map quality of mobile mappers, the time is coarsely discretized and the scene is described by features, i.e., local planar patches. This results in a partition of the trajectory into sub-scans that are treated rigidly. Then rigid registration algorithms like the ICP and other solutions to the SLAM problem are employed. Obviously, trajectory errors within a sub-scan cannot be improved in this fashion. Applying rigid pose estimation to this non-rigid problem directly is also problematic since rigid transformations can only approximate the underlying ground truth. When a finer discretization is used, single 2D scan slices or single points result that do not constrain a 6 DoF pose sufficiently for rigid algorithms.

More mathematical details of our algorithm in the available open-source code and are given in (Elseberg et al., 2013). Essentially, the algorithm first splits the trajectory into sections, and matches these sections using the automatic high-precision registration of terrestrial 3D scans, i.e., globally consistent scan matching that is the 6D SLAM core. Here the graph is estimated using a heuristic that measures the overlap of sections using the number of closest point pairs. After applying globally consistent scan matching on the sections the actual continuous-time or semi-rigid matching as described in (Elseberg et al., 2013) is applied, using the results of the rigid optimization as starting

values to compute the numerical minimum of the underlying least square problem. To speed up the calculations, the algorithm exploits the sparse Cholesky decomposition by (Davis, 2006).

Given a trajectory estimate, the point cloud is "unwound" into the global coordinate system and use nearest neighbour search to establish correspondences at the level of single scans (those can be single 2D scan profiles). Then, after computing the estimates of pose differences and their respective covariance, the algorithm optimizes the trajectory. In a pre-dependent step, trajectory elements every k steps are considered and l trajectory elements around these steps are fused temporarily into a meta-scan.

A key issue in continuous-time SLAM is the search for closest point pairs. An octree and a multi-core implementation using OpenMP is used to solve this task efficiently. A time-threshold for the point pairs is used, i.e., the algorithm matches only to points if they were recorded at least t_d time steps away.

Finally, all scan slices are joined in a single point cloud to enable efficient viewing of the scene. The first frame, i.e., the first 3D scan slice from the PUCKs scanner defines the arbitrary reference coordinate system.

5 Results

Results were obtained in an experiment at K+S KALI GmbH, Werk Werra. The system acquired a large scale 3D point cloud, that is compared to other state of the are mine mapping systems. Figure 1 presents the mapping system. It consists of a spinning RIEGL scanner and several 2D SICK LMS200 profilers. Figure 2 shows the 3D point cloud and Figure 3 shows the acquired point cloud (white) overlaid to an existing map. A flight through the acquired point is given in the following video: https://youtu.be/ntSlOMnNMF4

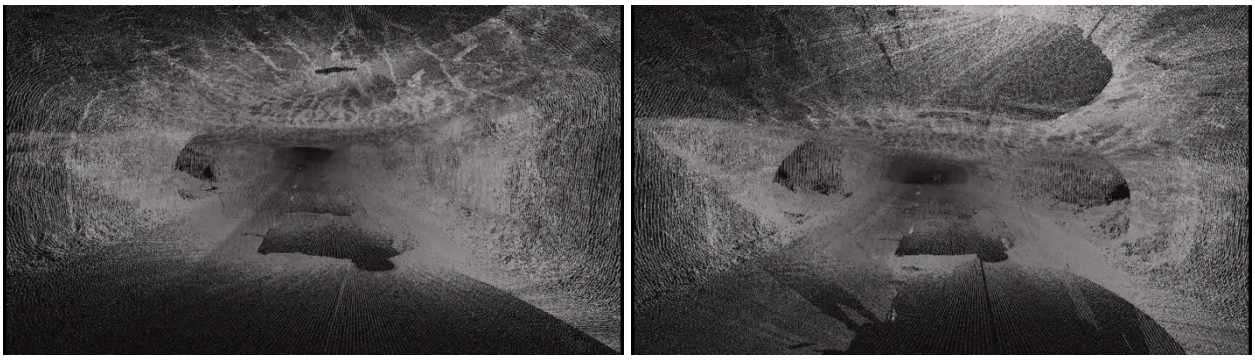

Fig. 2: 3D point cloud views of the mine.

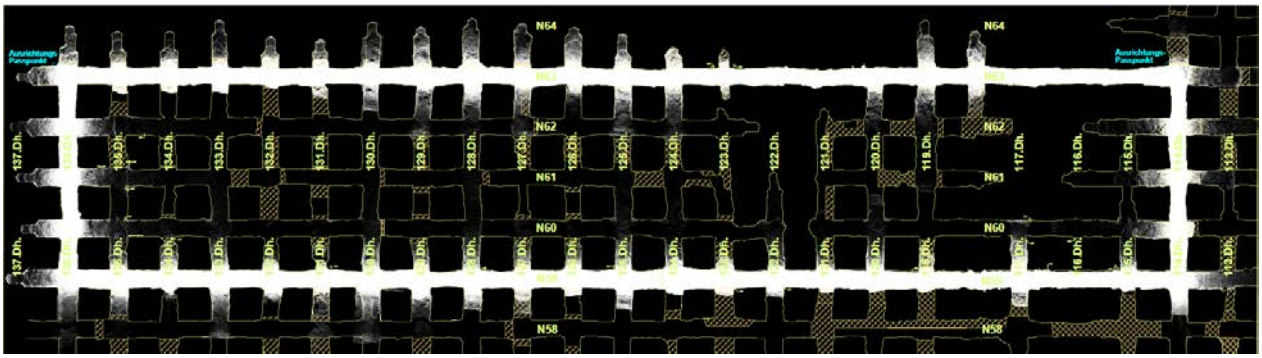

Fig. 3: 3D point cloud overlay with the existing map.

REFERENES

Besl, P. and McKay, D., 1992. A Method for Registration of 3–D Shapes. *IEEE Transactions on Pattern Analysis and Machine Intelligence (PAMI)*, 14(2):239–256, February.

Borrmann, D., Elseberg, J., Lingemann, K., Nüchter, A., and Hertzberg, J., 2008. Globally consistent 3D mapping with scan matching. *Journal Robotics and Autonomous Systems (JRAS)*, 56(2):130–142, February.

Bosse, M. and Zlot, R., 2009. Continuous 3D Scan-Matching with a Spinning 2D Laser. *In Proceedings of the IEEE International Conference on Robotics and Automation (ICRA '09)*, pages 4312–4319, May.

Davis, T. A., 2006. *Direct Methods for Sparse Linear Systems*. SIAM.

Durrant-Whyte, H. and Bailey, T., 2006. Simultaneous localization and mapping (slam): Part i. IEEE Robotics and Automation Magazine (RAM), 13(2):99-108, 2006.

Elseberg, J., Borrmann, D., and Nüchter, A., 2013. Algorithmic solutions for computing accurate maximum likelihood 3D point clouds from mobile laser scanning platforms. *Remote Sensing*, 5(11):5871–5906, November.

Hähnel, D., Burgard, W., Fox, D., and Thrun S., 2003. An efficient fastslam algorithm for generating maps of large-scale cyclic environments from raw laser range measurements. In *Proceedings of the IEEE/RSJ International Conference on Intelligent Robots and Systems (IROS'03)*, Las Vegas, Nevada, USA, October.

item24 Industrietechnik, 2017. Alu-Profilsystem-Baukasten für industrielle Anwendungen, 2015. http://www.item24.de/ .

Kohlbrecher, S., Meyer, J., von Stryk, J., and Klingauf, U., 2011. A flexible and scalable slam system with full 3d motion estimation. In *Proceedings of the IEEE International Symposium on Safety, Security and Rescue Robotics (SSRR ' 11)*, November.

Lucas, B. D. and Kanade T., 1981. An iterative image registration technique with an application to stereo vision. In Proceedings of the DARPA Image Understanding Workshop, pages 121-130, April.

Montemerlo, M., Thrun, S., Koller, D., Wegbreit B., 2002. Fastslam: A factored solution to the simultaneous localization and mapping problem. *In Proceedings of the AAAI National Conference on Artificial Intelligence (AAAI'02)*, pages 593-598. AAAI.

Nüchter, A., Elseberg, J., Borrmann, D., 2013. Irma3D – An Intelligent Robot for Mapping Applications. In Proceedings of the 3rd IFAC Symposium on Telematics Applications (TA'13), pages 119-124, Seoul, Korea, November.

Nüchter, A., Elseberg, J., Schneider, P., Paulus, D. 2010. Study of Parameterizations for the Rigid Body Transformations of The Scan Registration Problem. *Journal Computer Vision and Image Understanding (CVIU)*, 114(8):963-980, August 2010.

Nüchter, A., Surmann, H., Lingemann, K., Hertzberg, J., and Thrun S., 2004, 6D SLAM with an Application in Autonomous Mine Mapping. In Proceedings of the IEEE International Conference on Robotics and Automation (ICRA â€™04), pages 1998â€“2003, New Orleans, USA, April 2004.

Sheehan, M., Harrison, A., Newman, P., 2011. Self-calibration for a 3D Laser. The International Journal of Robotics Research, 31(5):675-687, 2011.

Stoyanov, T. and Lilienthal, A. J., 2009. Maximum Likelihood Point Cloud Acquisition from a Mobile Platform. In *Proceedings of the IEEE International Conference on Advanced Robotics (ICAR '09)*, pages 1– 6, June 22–26.